

Structural characteristics of M-type Ba-Sr hexaferrite nanoparticles prepared using sol-gel method: role of the Sr-ion concentrations and annealing temperatures

Sabah M. Ali Ridha and Mohammad A. Awad

¹Department of Physics/College of Education for Pure Sciences/ University of Kirkuk, Kirkuk, Iraq.

Email: sabahyagmur@uokirkuk.edu.iq

Email: mohammadaliawad@uokirkuk.edu.iq

Article history: Received: 14 July 2021, Revised: 25 August 2021, Accepted: 01 October 2021;

Abstract

Strontium substituted M-type Barium hexagonal ferrite $Ba_{1-x}Sr_xFe_{12}O_{19}$ ($x= 0, 0.1, 0.3, 0.5, 0.7, 0.9, 1.0$) has been synthesized via Sol-gel autocombustion method. This method has the potential to produce nanoparticle materials at low temperatures. The thermal decomposition of the autocombustion product verified by thermogravimetric (TGA) and differential thermal analysis (DTA). To obtain the hexagonal ferrite phase, the required annealing temperature estimated by TGA analysis. The fine powders produced by autocombustion at different temperatures (400, 600, and 800 °C) were annealed for three hours. The influence of annealing temperature on the structural characteristics of Ba-Sr ferrite was investigated in detail by using XRD, and SEM. The XRD results showed that increasing the annealing temperature leads to a decrease in the proportion of the intermediate phase such as $\gamma-Fe_2O_3$, $\alpha-Fe_2O_3$, and $BaFe_2O_4$ phases, while increasing the phase ratio of ferrite $BaFe_{12}O_{19}$. Whereas the ferrite phase, $BaFe_{12}O_{19}$, increases and exists as the single-phase at a temperature above 800 °C. The average crystallite size calculated from Debye-Scherrer's law lies in the range of (27-46 nm). While Lattice parameters of Ba-Sr ferrite found to increase linearly with increasing Sr-ion content, whereas the particle size estimated from SEM it found to increase with increasing Sr-ion concentration in the range of (27-48nm).

Keywords: Ba-Sr nanoferrite, SEM, Nanoparticles (NPs), sol-gel autocombustion, M-type hexaferrites, crystallite size.

Introduction

Ferrites have been widely used as permanent magnets due to their excellent chemical stability, low production cost, and acceptable magnetic performance [1]. Hexagonal ferrites (hexaferrite) occupies an important area of magnetic materials that have a much higher electrical resistance than metallic ferromagnetic materials, which can attenuate the incident electromagnetic waves and reduce eddy current losses [2]. M-type hexagonal ferrite belongs to the group of ferrimagnetic oxides and takes the chemical formula $(MFe_{12}O_{19})$ where M refers to divalent cations such as Ba^{+2} , Pb^{+2} or Sr^{+2} [3-5]. M-type hexagonal ferrite has a dense and compact crystal structure, where small iron ions Fe^{+3} are placed in the interstitial sites, while the oxygen O^{-2} , barium Ba^{+2} and strontium Sr^{+2} ions are distributed in sites inside the crystal lattice. Ferrites can be classified into four main groups based on their different crystalline structures, named; hexagonal [6], spinel [7], orthoferrite [8], and garnet ferrites [9].

According to the chemical formula and crystal structure, Barium hexaferrite (BHF) can be divided into six types and these types are; M-type ($BaFe_{12}O_{19}$), Z-type ($Ba_3Me_2Fe_{24}O_{41}$), Y-type ($Ba_2Me_2Fe_{12}O_{22}$), W- type ($BaMe_2Fe_{16}O_{27}$), X-type ($Ba_2Me_2Fe_{28}O_{46}$) and U- type ($Ba_4Me_2Fe_{36}O_{60}$), where "Me" can be inserted with the elements of Sr, Co, Ni or Zn [10].

The manufacture of BHF ceramics requires materials possessing high magnetic anisotropy, high saturation magnetization, high Curie temperature, and high natural resonance frequency with excellent ability and corrosion resistance. Due to its intrinsic magneto-crystalline anisotropy field, BHF

ceramics can be use at much higher frequencies than spinel ferrites and garnets [11-14].

BaFe₁₂O₁₉ has the greatest physical and chemical characteristics permitting it to be use in many applications, such as microwave device filters [15], magnetic recording materials [16], permanent magnet [17], and magneto-optics [18]. There are some conditions of the ferrite materials to be use in such applications, such as chemical stability, natural resonance frequency, ability to attenuate unwanted signals, high saturation magnetization, and high magnetic anisotropy. Therefore BaFe₁₂O₁₉ has been synthesized by coprecipitation, micro-emulsion, glass crystallization, citrate-precursor, microwave and hydrothermal, sol-gel, ball milling, and others [19–31].

Hexagonal M-type ferrite have been prepared with nanosize particles in order to increase the specific surface area of the particles and improve the absorption capacity per unit mass, which is suitable for practical application in absorbent materials and microwave protection[15]. Thus, increasing the volume/area ratio will greatly improve the physical and chemical properties of nanometer-sized materials, which differ significantly from those of micron-sized materials. Therefore, investigation of the dielectric properties and electrical conductivity at different frequencies will give useful data about the mechanism of conduction in ferrite [32].

A number of studies have been investigated on the partial substitutions were done for the cation in the M-type hexaferrite in order to improve the electrical and magnetic properties, and a result to improve the microwave frequency characteristics in these materials. Many divalent cations such as Co⁺², Mn⁺², Cu⁺², Zn⁺², Ni⁺² and tetravalent cations such as Ti⁺⁴, Zr⁺⁴, Ir⁺⁴, Ru⁺⁴ were used either separately or in the form of multi-cations substitutions[33-37].

In in the present work, we have synthesis the Ba_{1-x}Sr_xFe₁₂O₁₉ with (x = 0.0, 0.1, 0.3, 0.5, 0.7, 0.9, and 1.0) nano-hexaferrites by using sol-gel autocombustion technique, which is an efficient cost effective process over other conventional preparation methods, with short synthesis time and results single domain nanosize particles. In addition to that, an effect of Sr⁺² concentration on the morphological and structural properties of Ba_{1-x}Sr_xFe₁₂O₁₉ nanomaterials were investigate. The structural and morphological properties of the ferrite nanoparticles can studied by using XRD, and SEM analyses.

Experimental

The M-type of Strontium substituted Barium hexaferrite Ba_{1-x}Sr_xFe₁₂O₁₉ nanoparticles (were, x= 0.0, 0.1, 0.3, 0.5, 0.7, 0.9, 1.0) were synthesized via sol-gel autocombustion technique. The starting materials were taken as Analytical grade of barium nitrate Ba(NO₃)₂ (99% Merck, India), strontium nitrate Sr(NO₃)₂ (99% Merck, India), iron nitrate Fe(NO₃)₃ .9H₂O (98%Merck, India), citric acid C₆H₈O₇ .H₂O (99% Merck, India), and Ammonia solution. Iron, barium, and strontium nitrates are mixed and dissolve it in an appropriate amount of distilled water to make a mixture of nitrates solution with stoichiometric proportions and mole ratio Fe/(Ba + Sr) of (12:1). Afterward, Citric acid was dissolved in a distilled water and added dropwise into the metallic nitrates solution to chelate Ba⁺², Sr⁺², and Fe⁺³ ions in the solution with constant magnetic stirring at 300 rpm. The metal nitrates to citric acid mole ratio were kept at 1:1, then the pH of the final mixed solution kept at (7) by adding ammonia solution in the form of drops with continuous stirring, as a result we observed the formation of a homogenous brown colored solution. The final solution was vaporize to dryness during the heating in the range of 90-100 °C on a hot plate with continuous stirring. When the water evaporated, the solution became viscous gel and convert to a viscous brown gel. Yellow combustion flame has appeared when the temperature reaches 180 °C. Increasing the temperature to 200-220 °C leads to the ignition of the dried gel. The dried gel burnt by autocombustion until fully complete to form a brown-colored loose powder. The as-burnt ashes collected and ground to be ready for subsequent heating treatment. Depending on the decomposition pattern TG/DTA, all the resultant fine powders were calcined at different temperatures 400, 600, and 800 °C for 3h in muffle furnace in order to obtain the M-type of Ba-Sr hexaferrite phase. Figure (1) shows a flow chart of the synthesis procedure leading to the formation of Ba-Sr hexaferrite nanoparticles. Thermal decomposition behavior of the as prepared nanopowders studied using the simultaneous TG/DTA analysis as shown in figure (2). The phase of

the gel precursor, the as-burnt and calcined powders were investigated using X-ray diffraction (XRD) using Cu K α radiation ($\lambda = 1.5405 \text{ \AA}$). The average crystallite size of the powders was measured by the X-ray line-broadening technique employing the Debye-Scherrer equation, which used the FWHM of the (114) intense peak. The particle morphology and particle size distribution examined by SEM techniques.

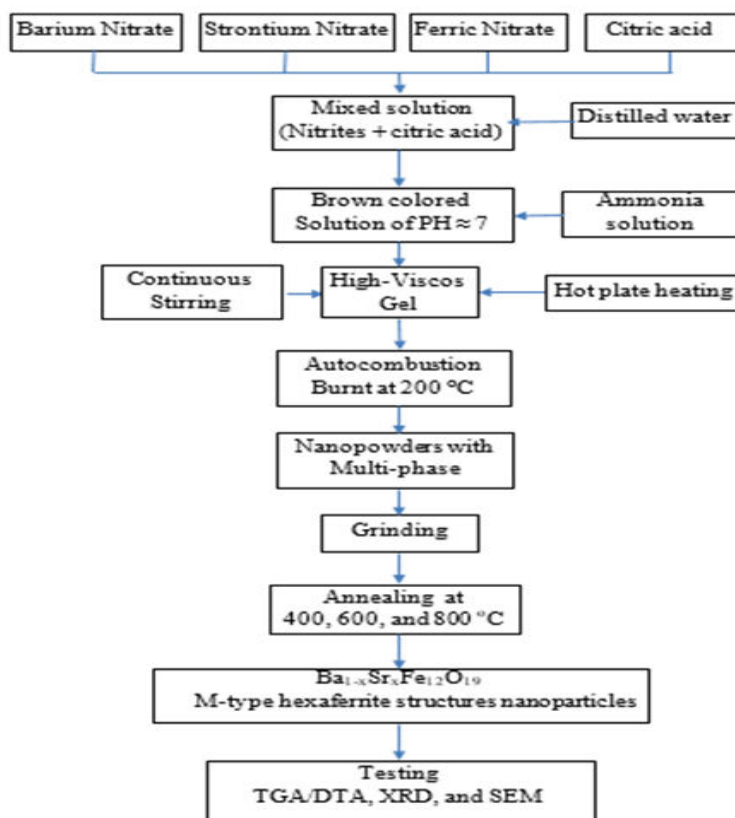


Figure 1: Flow chart of sol-gel autocombustion technique Ba- Sr M-type hexaferrite nanopowders.

Result and Discussion

Thermal Decomposition

The thermal decomposition, stability, and the temperature of phase formation study of Co-Ni ferrite powders with chemical composition of as-burnt $\text{Ba}_{0.5}\text{Sr}_{0.5}\text{Fe}_{12}\text{O}_{19}$ hexaferrite nanopowders is carried out by TG-DTA. The relative weight variations associated with the entropy variations during the heating of the nanopowders under air are shown in figure (2). Therefore, there is no weight increase observed, thus no oxidation process takes place under air for the prepared powder. Data is collected from the heating process at temperatures in the range of (25-1000 °C) with heating rate of 10 °C/min. Figure (2) shows the TG /DTA traces of the as-burnt powders. The DTA diagram shows four peaks, the endothermic peak at around 95 °C with a minor weight loss (1%), could correspond to the dehydration of the absorbing water of the as-burnt powders. The first exothermic peak at about 260 °C with a weight loss of 3% could be due to the decomposition of the unreacted citric acid that remained after combustion. The second exothermic peak at 685 °C with a weight loss of 3% might be attributed to the decarboxylation of BaCO_3 formed during combustion, which has been reported to take place at 680 °C for pure carbonate and at around 700 °C for a mixture of carbonate and an iron oxide [38]. This peak also could be assigned to simultaneous formation of mono-ferrite (BaFe_2O_4). The last broadened exothermic peak at 796 °C with very small weight loss (<0.1%) could be considered as a

solid-state reaction attributed to the gradual formation of barium hexaferrite. Chemical and structural changes, and the desired crystal phases present in the materials during combustion and annealing processes could be observed by characterization using different kind of spectrometers. This may be helpful in understanding the combustion reaction mechanism.

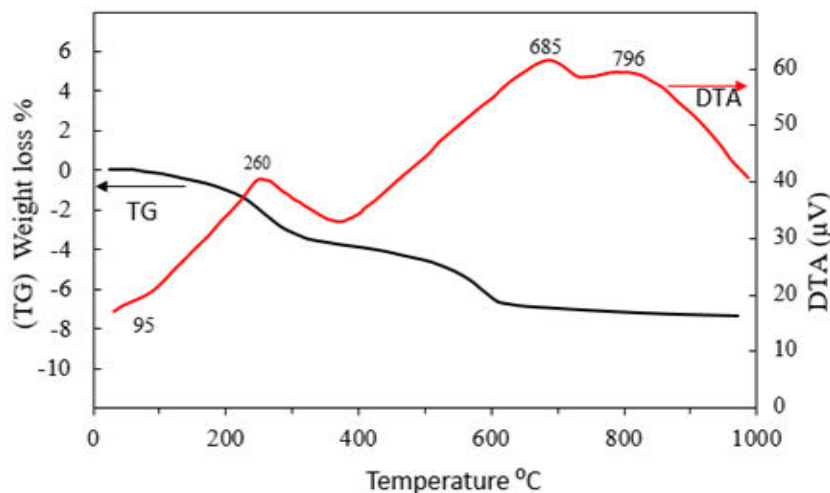


Figure 2: TG-DTA, decomposition pattern of the as-burnt $Ba_{1-x}Sr_xFe_xFe_{12}O_{19}$ M-type hexaferrite nanopowders.

X-ray Diffraction analysis

Figure (3) illustrates the powder XRD patterns of as prepared sol-gel combustion product (as burnt) of BaM ferrite nanopowders, and subsequently annealed at different temperatures 400, 600 and 800 °C for three hours. The standard XRD pattern of BaM phase is present at the bottom side of the figure (3). The annealing temperatures influence the crystallinity and phase purity of the powders.

The XRD pattern of as-burnt powders (Figure 3) clearly indicates that the expected $BaFe_{12}O_{19}$ phase disappears in the combustion process. At the same time, it indicates the presence of $\gamma-Fe_2O_3$ as a major phase and some other minor phases. As temperature increases to about 400°C, the $\gamma-Fe_2O_3$ phase converts into $\alpha-Fe_2O_3$ as the dominant phase.

By increasing the annealing temperature to about 600°C, most of $\alpha-Fe_2O_3$ pattern peaks disappear and the $BaFe_{12}O_{19}$ appears (because of the reaction between the $BaFe_2O_4$ and $\alpha-Fe_2O_3$ phases) as a dominant phase over the other phases. $BaFe_{12}O_{19}$ peaks indexed to the (110), (114), (108), (2011) and (220) planes, while only one peak of the $BaFe_2O_4$ phase remains at the angle of 28.55°. However, when the annealing temperature increases to about 800°C, it improves and grows the crystalline nature of $BaFe_{12}O_{19}$ ferrite as a complete single phase with peaks indexed to the (102), (104), (110), (107), (114), (108), (203), (205), (206), (1011), (209), (217), (2011), (220), (2014), and (1116) planes at angles in the range of (18-73°). While the main intense peak of the resulting ferrite is (114) at an angle of 34.38°, as shown in figure (3).

The XRD patterns of the hexaferrite powders $Ba_{1-x}Sr_xFe_xFe_{12}O_{19}$ ($x = 0.0, 0.1, 0.3, 0.5, 0.7, 0.9$ and 1) annealed at 800°C for three hours are shown in Figure (4). It should be noted that no $\alpha-Fe_2O_3$ phase was detected. All the major peaks in the diffraction patterns indexed to various (hkl) planes (102), (006), (110), (107), (114), (108), (203), (205), (206), (209), (2010), (2011), (218), (220), (313), and (228) at angles in the range of (18-73°). This figure shows that the intense main peak (114) has a wide FWHM of the $Ba_{1-x}Sr_xFe_xFe_{12}O_{19}$ samples, which indicates the shift of the XRD peak (114) towards the higher angles, with increasing strontium content. Displacement of the peaks is due to the reduction in the lengths of the Fe-O bond, the angle of the Fe-O-Fe bond and the volume of the elementary cell.

All samples showed well-defined Bragg peaks, intense and sharp, indicating the crystalline nature of the samples.

Phase identification of Ba-Sr hexaferrite nanopowders is carried out by XRD with Cu-K α radiation ($\lambda = 1.54056 \text{ \AA}$) in 2θ range 15–80°.

The Bragg's law is written as:

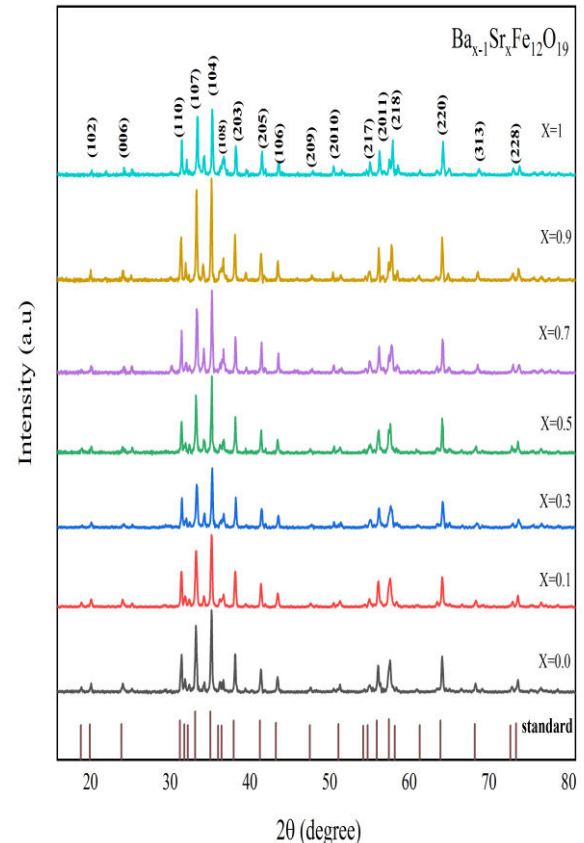
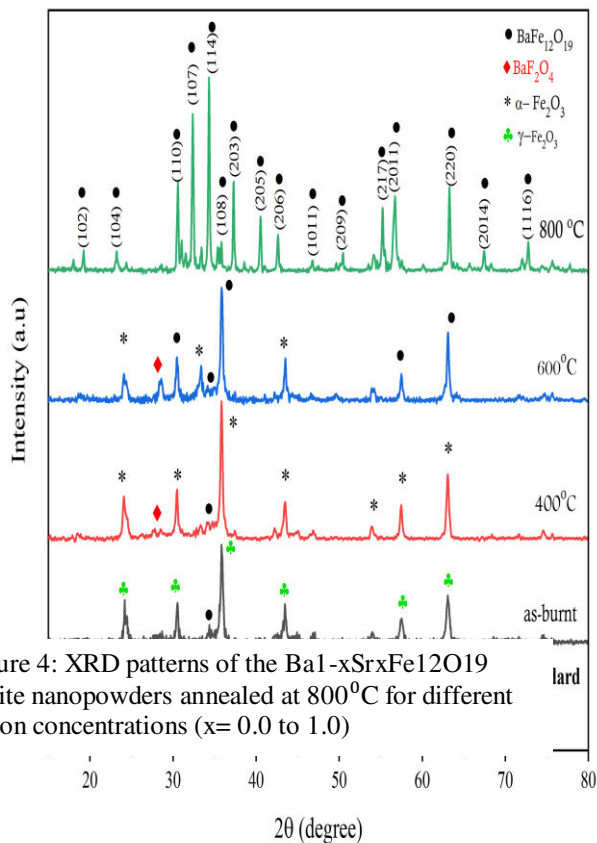


Figure 4: XRD patterns of the Ba_{1-x}Sr_xFe₁₂O₁₉ ferrite nanopowders annealed at 800°C for different Sr-ion concentrations (x= 0.0 to 1.0)

Figure 4: XRD patterns of the Ba_{1-x}Sr_xFe₁₂O₁₉ ferrite nanopowders annealed at 800°C for different Sr-ion concentrations (x= 0.0 to 1.0)

$$n\lambda = 2d \sin\theta \dots\dots\dots(1)$$

where, d is the spacing between the atomic planes, θ is the half-value of the diffraction angle, n is the order of the reflection.

The value of the full-width at half-maximum of the strongest intensity diffraction peak (114) was used to calculate the crystallites size using Debye-Scherrer's equation;

$$t = \frac{k\lambda}{\beta \cos\theta} \dots\dots\dots(2)$$

Where, β is integral breadth (in radians), and K is Scherrer's constant its value is 0.9 [39];

The lattice parameters a and c are calculated using the following equation [40]:

$$d_{hkl} = \left(\frac{4(h^2+hk+k^2)}{3a^2} + \frac{l^2}{c^2} \right)^{-1/2} \dots\dots\dots(3)$$

where d_{hkl} is the crystal face distance and (hkl) are the Miller indices.

The unit cell volume for barium hexaferrite can be estimated using the lattice parameters a and c from the

following relation (41):

$$V = \frac{\sqrt{3}}{2} a^2 c \dots\dots\dots (4)$$

The theoretical (X-ray) density (d_x) of the prepared powders are determined by applying the equation:

$$d_x = \frac{ZM_{wt}}{N_A V} \dots\dots\dots(5)$$

where $Z = 2$ indicating 2 formula units M_{wt} is material molecular weight and N_A is Avogadro's number.

All the above X-ray characteristic parameters of the $Ba_{1-x}Sr_xFe_{12}O_{19}$ hexaferrite nanoparticles calcined at 800 °C are listed in table (1), and were calculated using the standard relations shown in equations (1-5).

Table 1: X-ray parameters; (Lattice parameters a and c),
t (crystallite size), d_x (x-ray density), For $Ba_{1-x}Sr_xFe_{12}O_{19}$
hexaferrites at deferent Sr- ion concentrations

Sr-ion concentration (x)	2θ (degree) peak 114	crystallite size t (nm)	lattice constant a (°Å)	lattice constant c (°Å)	c/a	X-ray density d_x (g/cm ³)
0	34.332	31.63	5.844	23.222	3.974	5.376
0.1	34.341	27.72	5.845	23.174	3.965	5.360
0.3	34.424	46.20	5.835	23.069	3.954	5.355
0.5	34.344	46.19	5.844	23.185	3.968	5.264
0.7	34.402	34.65	5.856	22.993	3.926	5.236
0.9	34.327	31.63	5.854	23.084	3.944	5.172
1	34.430	31.62	5.840	22.973	3.934	5.198

As shown in Table 1, the lattice constants of $Ba_{1-x}Sr_xFe_{12}O_{19}$ were found in the range of (5.835-5.856Å) for (a), and (22.97-23.22 Å) for (c) parameter. The variation of lattice constants (a) and (c) as a function of the Sr-ion concentration are shown in figure (5). The values of lattice constant (a) are slightly increasing while those of (c) are slightly decreasing with increasing of Sr-ion concentration and this can be attributed to the smaller ionic radius of Sr^{+2} (1.18Å) as compared with that of Ba^{+2} (1.35Å).

Figure (6) illustrates the crystallite size and x-ray density variations with Sr-ion concentration of the Ba-Sr ferrite nanopowders. The crystallite size of Sr-ferrite is similar to that of Ba-ferrite, but the increase in the Sr-ion concentration increases the crystallite size of $Ba_{1-x}Sr_xFe_{12}O_{19}$ while it reaches its highest value (46 Å) at $x=0.5$, due to the presence of the strontium ion next to the barium, which accelerates the growth of crystallite sizes. While X-ray density decreases linearly with increasing Sr-ion concentration. This is due to the ionic radius Sr^{+2} is smaller than that of Ba^{+2} ion, since the X-ray density is directly proportional to the molecular weight of the ferrite sample.

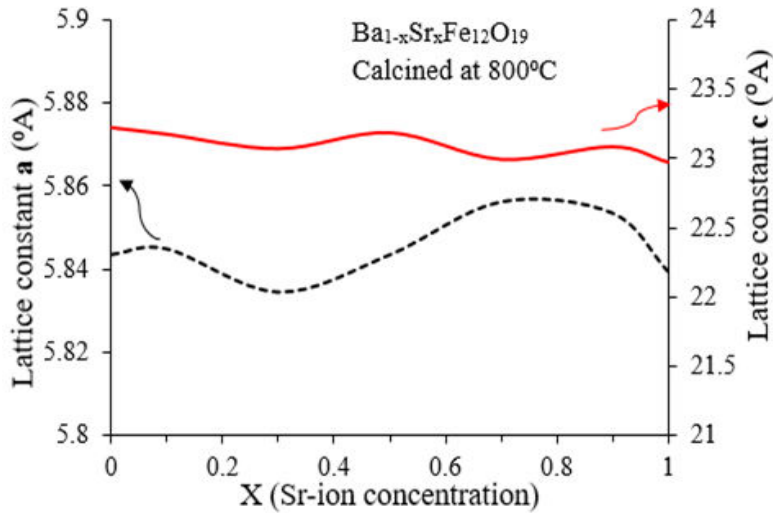


Fig. 5: lattice constants (a) and (c) versus Sr-ion concentration of $Ba_{1-x}Sr_xFe_{12}O_{19}$ annealed at 800 °C

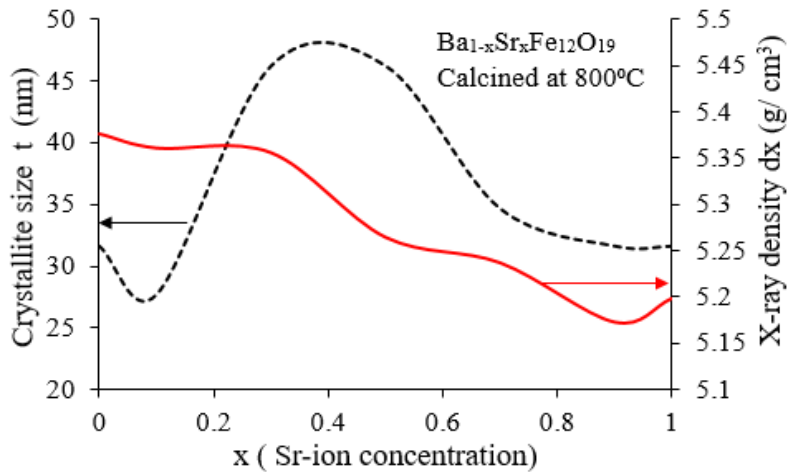


Fig. 6: x-ray density and crystallite size versus Sr-ion concentration of $Ba_{1-x}Sr_xFe_{12}O_{19}$ annealed at 800 °C

Scanning Electron Microscopy (SEM)

The SEM images of the synthesized powders of $BaFe_{12}O_{19}$, $Ba_{0.5}Sr_{0.5}Fe_{12}O_{19}$ and $SrFe_{12}O_{19}$ ferrites all annealed at 800 °C for three hours as a function of Sr-ion concentrations(x) are shown in Figure (7-a, -b and -c). The Most of grains found to be relatively well-defined semi spherical in shape and are

homogeneously distributed. All the micrographs are of ultra-fine with the individual particle size less than 50 nm. Table (2) shows that the average crystallite size as calculated from XRD by Scherer equation is approximately equal to the average particle size derived from SEM measurements. Moreover, there is a little difference in the particle size obtained by increasing the Sr-ion concentration.

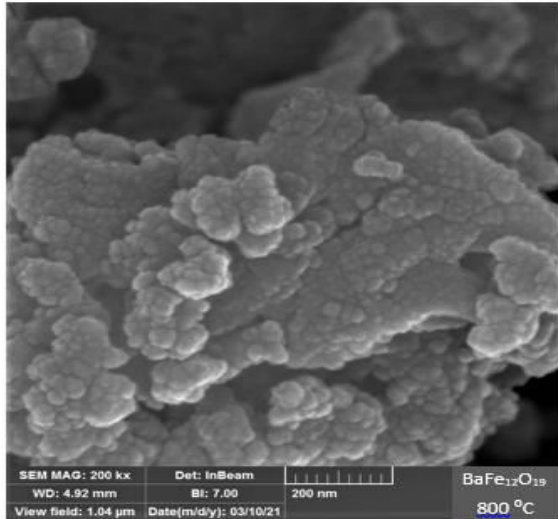


Fig. 7-a: SEM images of BaFe₁₂O₁₉ ferrite nanopowders for annealed at 800°C.

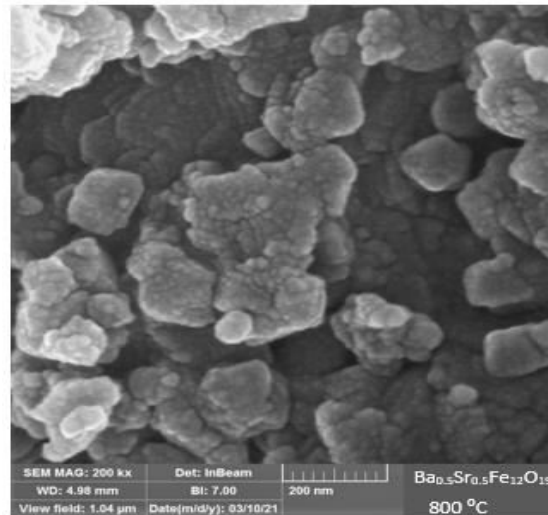


Fig. 7-b: SEM images of Ba_{0.5}Sr_{0.5}Fe₁₂O₁₉ ferrite nanopowders for annealed at 800°C.

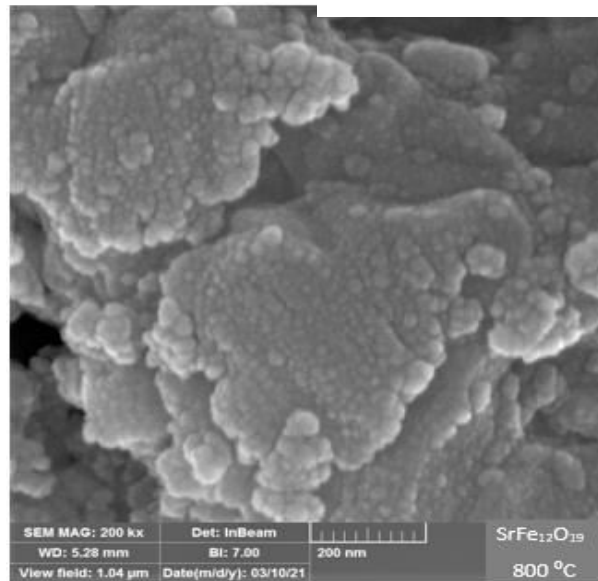


Fig. 7-c: SEM images of SrFe₁₂O₁₉ ferrite nanopowders for annealed at 800°C.

Table 2: average particle size (t_{SEM}) and average crystallite size (t_{XRD}) for $BaFe_{12}O_{19}$, $Ba_{0.5}Sr_{0.5}Fe_{12}O_{19}$ and $SrFe_{12}O_{19}$ annealed at temperature $800^{\circ}C$ for 3 hours

Ferrite	Average particle size (t_{SEM}) nm	Average Crystallite size (t_{XRD}) nm
$BaFe_{12}O_{19}$	27-37	31.63
$Ba_{0.5}Sr_{0.5}Fe_{12}O_{19}$	39-48	46.19
$SrFe_{12}O_{19}$	26-40	31.62

Conclusions

Barium-Strontium hexaferrite nanopowders with chemical formula of $Ba_{1-x}Sr_xFe_{12}O_{19}$ (where, $x= 0.0, 0.1, 0.3, 0.5, 0.7, 0.9, 1.0$) were successfully synthesized using sol-gel auto combustion method and annealed at temperatures (as-burnt, $400, 600, 800^{\circ}C$). The thermal decomposition, stability, and the temperature of phase formation studied by TG/DTA, while the effect of annealing temperatures on crystallinity, phase composition and morphology was investigate by various characterization methods, i.e., XRD and SEM respectively. XRD displayed that all samples exhibited the characteristic behavior of single phase M-type (Ba-Sr) hexaferrite nanoparticle annealed at $800^{\circ}C$, but the annealed powders at 400 and $600^{\circ}C$ consist of several different phases, such as $\gamma-Fe_2O_3$ at as-burnt powders, $\alpha-Fe_2O_3$ with $BaFe_2O_4$ phases at $400^{\circ}C$. The hexaferrite phase begins to grow through the reaction of $\alpha-Fe_2O_3$ with $BaFe_2O_4$ phases and clearly appears at $600^{\circ}C$. The crystallite size, lattice parameters x-ray density found to be dependent on the Sr-ion concentration and annealing temperatures. SEM images clearly showed that the crystallite size (calculated from the Debye-Scherrer's law) and particle size (measured by SEM) increases as the annealing temperatures increases, while they decreases as the Sr-ion concentration increases.

References

- [1] F. Shaikh, M. Ubaidullah, R. S. Mane and A. M. Al-Enizi, Spinel Ferrite Nanostructures for Energy Storage Devices Micro and Nano Technologies, Types, Synthesis methods and applications of ferrites, Ch. 4, pp. 51–82, 2020.
- [2] F. G. da Silva, J. Depeyrot, A. F. Campos, R. Aquino, D. Fiorani and D. Peddis, Structural and Magnetic Properties of Spinel Ferrite Nanoparticles, Journal of Nanoscience and Nanotechnology, Vol.19, No. 8, pp. 4888-4902, 2019. doi: 10.1166/jnn.2019.16877
- [3] V. Denis A. and et al , Magnetic and Structural Properties of Barium Hexaferrite $BaFe_{12}O_{19}$ from Various Growth Techniques, Materials, Vol. 10, pp. 1-11, 2017. doi:10.3390/ma10060578
- [4] N. B. Ibrahim, Y. Noratiqah, M. F. Jailani, and E. R. Iruthayaraj, Improved structural and magnetic properties of a non-stoichiometry Ba:Fe ratio of barium hexaferrite film, Materials Science and processing, Applied Physics A, Vol. 126, No. 11, pp. 1-8, 2020 doi: 10.1007/s00339-020-04075-3
- [5] R. A. Nandotaria, R. B. Jotania, and C. C. Chauhan, Effect of Lead substitution On The Microstructural, Magnetic and Dielectric Properties of Barium Hexaferrite Powder,

- International Journal of Latest Technology in Engineering, Management & Applied Science (IJLTEMAS), Vol. 3, No. 4A, pp. 56-61, 2014.
- [6] A. D. Suwandi, and et al., Comparison of crystalline structure and magnetic properties in $PbAl_xFe_{12-x}O_{19}$ synthesized by coprecipitation and sonochemistry, 10th International Conference on Physics and Its Applications (ICOPIA 2020), Journal of Physics: Conference Series 1825 (2021) 012043 , [https:// doi:10.1088/1742-6596/1825/1/012043](https://doi.org/10.1088/1742-6596/1825/1/012043)
- [7] S. M. Hussein, T.H. Mubarak, S.M. Ali Ridha, and J. Al-Zanganawee. Synthesis and Studying Induction Heating of $Mn_{1-x}Zn_xFe_2O_4$ ($x=0- 0.5$) Magnetic Nanoparticles for Hyperthermia Treatments, Key Engineering Materials, Vol. 882, pp. 200-218, April 2021.
- [8] I. Purnamasari, I. Farida, N. Nanang and A. Zhafirah, Crystal structure analysis of Lanthanum Orthoferrite doped Zirconium with sol-gel method for solar cell candidate, Annual Conference on Science and Technology (ANCOSSET 2020), Journal of Physics: Conference Series; Volume 1869, 2021. [https:// doi:10.1088/1742-6596/1869/1/012197](https://doi.org/10.1088/1742-6596/1869/1/012197)
- [9] M. N. Smirnova, I. S. Glazkova, et al., Synthesis of Ce:YIGnanopowder by gel combustion, Nanosystems: Physics, Chemistry, Mathematics, Vol. 12, No. 2, Pp. 210–217, 2021 [https://doi: 10.17586/2220-8054-2021-12-2-210-217](https://doi.org/10.17586/2220-8054-2021-12-2-210-217)
- [10] B. Jotania, R. B. Khomane, A. S. Deshpande, C. C. Chauhan and B. D. Kulkarni, Physical and Magnetic Properties of Barium Calcium Hexaferrite Nano-particles Synthesized by Water-in-oil Reverse Micelle and Co-precipitation Techniques, Journal of Science Research, Vol. 1, No. 1, pp. 1-13, 2009. [https:// doi.org/10.3329/jsr.v1i1.1684](https://doi.org/10.3329/jsr.v1i1.1684)
- [11] E. Roohani, and et al., Effect of annealing temperature on structural and magnetic properties of strontium hexaferrite nanoparticles synthesized by sol-gel auto-combustion method, International Journal of Modern Physics B, Vol. 29, pp. 1-11, 2015.[https://doi: 10.1142/S0217979215501908](https://doi.org/10.1142/S0217979215501908)
- [12] T. Sembiring, Y. B. Zebua and Muljadi, Analysis of crystal structure and magnetic character strontium ferrite ($SrFe_{12}O_{19}$) powder made of stoichiometry and nonstoichiometric compositions, AIP Conference Proceedings Vol. 2221, No. 1, pp. 1-5, 2020. <https://doi.org/10.1063/5.0005232>
- [13] S. V. Trukhanov, and et al., Investigation into the structural features and microwave absorption of doped barium hexaferrites, Dalton Transactions, Vol. 46, pp. 9010-9021, 2017. doi: 10.1039/C7DT01708A
- [14] S. K. Godara, and et al., Tailoring the magnetic properties of M-type strontium ferrite with synergistic effect of co-substitution and calcinations temperature, Journal of Asian Ceramic Societies, Vol. 9, No. 2, 2021. doi.org/10.1080/21870764.2021.1911059
- [15] Y. Marouani, and et al., Electrical conductivity and dielectric properties of Sr doped M-type barium hexaferrite $BaFe_{12}O_{19}$, Royal Society of Chemistry advances, Vol. 11, pp. 1531–1542, 2021. [https://doi: 10.1039/d0ra09465j](https://doi.org/10.1039/d0ra09465j)
- [16]] A. R. Al Dairy, L. A. Al-Hmoud, and H. A. Khatatbeh, Magnetic and Structural Properties of Barium Hexaferrite Nanoparticles Doped with Titanium, Symmetry, Vol. 11, pp. 1-12, 2019. [https:// doi:10.3390/sym11060732](https://doi.org/10.3390/sym11060732)
- [17] K. Chahal and K. S. Samra, Magnetic and dielectric behavior of praseodymium substituted barium hexaferrite, Journal of Alloys and Compounds, Vol. 737, pp. 387-391, 2018. [https:// doi.org/10.1016/j.jallcom.2017.12.056](https://doi.org/10.1016/j.jallcom.2017.12.056)
- [18] T. Shiratsu and H. Yao, Size dependence of magneto-optical activity in silver nanoparticles with dimensions between 10 and 60 nm studied by MCD spectroscopy, Physical Chemistry

- Chemical Physics, Vol. 20, pp. 4269-4276, 2018. <https://doi.org/10.1039/C7CP07695A>
- [19] M. K. Dmour, and et al., Structural and Magnetic Properties of Ba_{1-x}RexCo₂ZnxFe_{16-x}O₂₇ W-type Hexaferrite prepared by Ball Milling Method, Material Science Research India, Vol.17, No. 1, Pp. 34-46, 2020 doi.org/10.13005/msri/170106
- [20] K. Sadhana , K. Praveena , S. Matteppanavar and B. Angadi , Structural and magnetic properties of nanocrystalline BaFe₁₂O₁₉ synthesized by microwave-hydrothermal method, Applied Nanoscience, Vol. 2, pp. 247–252, 2012. [https://doi: 10.1007/s13204-012-0100-1](https://doi.org/10.1007/s13204-012-0100-1)
- [21] D. Lisjak and M. Drogenik, The Low-Temperature Formation of Barium Hexaferrites, Journal of the European Ceramic Society, Vol. 26, No. 16, pp. 3681-3686, 2006.[https://doi: 10.1016/j.jeurceramsoc.2005.12.014](https://doi.org/10.1016/j.jeurceramsoc.2005.12.014)
- [22] S.V. Trukhanov, A. V. Trukhanov, et al., Effect of gallium doping on electromagnetic properties of barium hexaferrite, Journal of Physics and Chemistry of Solids, Vol. 111, pp. 142-152, 2017. <https://doi.org/10.1016/j.jpics.2017.07.014>
- [23] [23] R. H. Arabi, R. Sarhaddi, S. Sudkhah and A. Shabani, Effect of annealing temperature on structural and magnetic properties of strontium hexaferrite nanoparticles synthesized by sol–gel auto-combustion method, International Journal of Modern Physics B, Vol. 29, pp. 1-11, 2015. [https://doi:10.1142/S0217979215501908](https://doi.org/10.1142/S0217979215501908)
- [24] B. Want and B. Hamid, Magnetic and dielectric characteristics of Nd and Nd-Mg substituted strontium hexaferrite, Modern Electronic Materials, Vol. 4, no. 1, pp. 21-29, 2018.[https://doi: 10.3897/j.moem.4.1.33273](https://doi.org/10.3897/j.moem.4.1.33273)
- [25] K. Samikannu, J. Sinnappan, and et al , Synthesis and magnetic properties of conventional and microwave calcined strontium hexaferrite powder, Materials Sciences and Applications, Vol. 2, No. 6, pp. 638-642, 2011.
- [26] B. Agea-Blanco, S. Reinsch, and R. Müller, Sintering and Foaming of Barium Silicate Glass Powder Compacts, Frontiers in Materials, Vol. 3, article 45, pp. 1-10, 2016.<https://doi.org/10.3389/fmats.2016.00045>
- [27] S. Akhtar, S. Saba, and et al., Microemulsion-based synthesis of strontium hexaferrite cobalt iron oxide nanoparticles and their biocompatibility in albino mice, Journal of Experimental Nanoscience, Vol. 13, No. 1, pp. 199-211, 2018.<https://doi.org/10.1080/17458080.2018.1475759>
- [28] A. V. Trukhanov, K. A. Astapovich, and et al., Peculiarities of the magnetic structure and microwave properties in Ba(Fe_{1-x}Sc_x)₁₂O₁₉ (x<0.1) hexaferrites, Journal of Alloys and Compounds, Vol. 822, pp. 1-11, 2020.<https://doi.org/10.1016/j.jallcom.2019.153575>
- [29] T. H. Ting and K. H. Wu, Synthesis, characterization of polyaniline/BaFe₁₂O₁₉ composites with microwave-absorbing properties, Journal of Magnetism and Magnetic Materials, Vol. 322, No. 15, pp. 2160-2166, 2010.[https://doi: 10.1016/j.jmmm.2010.02.002](https://doi.org/10.1016/j.jmmm.2010.02.002)
- [30] I. Bsoul and S. H. Mahmood, Magnetic and structural properties of BaFe_{12-x}GaxO₁₉ nanoparticles, Journal of Alloys and Compounds, Vol. 489, No. 1, pp. 110-114, 2010.<https://doi.org/10.1016/j.jallcom.2009.09.024>
- [31] S. L. Hua, J. Liub, H. Y. Yuc, and Z. W. Liu, Synthesis and properties of barium ferrite nanopowders by chemical co-precipitation method, Journal of Magnetism and Magnetic Materials, Vol. 473, Pages 79-84, 2019. <https://doi.org/10.1016/j.jmmm.2018.10.044>
- [32] S. S. Satpute, and et al., Substitution effect of Y⁺³ ions on the structural, magnetic and electrical properties of cobalt ferrite nanoparticles, Cerâmica, Vol. 66, pp. 43-49, 2020. doi.org/10.1590/0366-69132020663772734

- [33] M. Rostami, M. Moradi, R.S. Alam, and R. Mardani, Effect of Substitution of Mn, Cu, and Zr on the Structural, Magnetic, and Ku-Band Microwave-Absorption Properties of Strontium Hexaferrite Nanoparticles, *Journal of Electronic Materials*, Vol. 45, No. 8, pp. 4154-4161, 2016. [https://doi: 10.1007/s11664-016-4635-x](https://doi.org/10.1007/s11664-016-4635-x)
- [34] A.R. Farhadizadeh, S.A. Seyyed Ebrahimi, and S.M. Masoudpanah, Magnetic and microwave absorption properties of ZnCo-substituted W-type strontium hexaferrite, *Journal of Magnetism and Magnetic Materials*, Vol. 382, pp. 233-236, 2015. doi.org/10.1016/j.jmmm.2015.01.069
- [35] M. Rostami, and et al., Structural, magnetic, and microwave absorption properties of Mg–Ti–Zr–Co-substituted barium hexaferrites nanoparticles synthesized via sol–gel auto-combustion method, *Journal of Sol-Gel Science and Technology*, vol. 82, pp.783–794 , 2017. [https://doi: 10.1007/s10971-017-4369-0](https://doi.org/10.1007/s10971-017-4369-0)
- [36] A. Kumar, M. Kumar Verma, and et al., Electrical, Magnetic and Dielectric Properties of Cobalt-Doped Barium Hexaferrite $BaFe_{12-x}Co_xO_{19}$ ($x = 0.0, 0.05, 0.1$ and 0.2) Ceramic Prepared via a Chemical Route, *Journal of Electronic Materials* vol. 49, pp. 6436–6447, 2020. <https://doi.org/10.1007/s11664-020-08364-8>
- [37] R. Shams Alam, M. Moradi, and H. Nikmanesh, Influence of multi-walled carbon nanotubes (MWCNTs) volume percentage on the magnetic and microwave absorbing properties of $BaMg_{0.5}Co_{0.5}TiFe_{10}O_{19}/MWCNTs$ nanocomposites, *Materials Research Bulletin*, Vol. 73, pp. 261-267, 2016. <https://doi.org/10.1016/j.materresbull.2015.09.016>
- [38] G. Benito, M. P. Morales, and et al., Barium hexaferrite monodispersed nanoparticles prepared by the ceramic method, *Journal of Magnetism and Magnetic Materials*, Vol. 234, No. 1, Pp. 65-72, 2001. [https://doi.org/10.1016/S0304-8853\(01\)00288-8](https://doi.org/10.1016/S0304-8853(01)00288-8)
- [39] J.H. Yang, L.Y. Zhao, and et al., Magnetic properties of Co-doped ZnO prepared by sol-gel method. *Materials Science and Engineering B*, Vol. 162, No. 3, pp. 143-146, 2009. [https://doi: 10.1016/j.mseb.2009.03.020](https://doi.org/10.1016/j.mseb.2009.03.020)
- [40] M. Barakat, D. Bakeer and A. Sakr, Structural, Magnetic Properties and Electron Paramagnetic Resonance for $BaFe_{12-x}Hg_xO_{19}$ Hexaferrite Nanoparticles Prepared by Co-Precipitation Method, *Journal of taibah university for sciences*, Vol. 14, No. 1, pp. 640–652, 2020. <https://doi.org/10.1080/16583655.2020.1761676>
- [41] [41] M.A. Almessiere, Y. Slimani, and N.A. Tashkandi, The effect of Nb substitution on magnetic properties of $BaFe_{12}O_{19}$ nano hexaferrites, *Ceramics International*, Vol. 45, No. 2, pp., 2018. [https://doi: 10.1016/j.ceramint.2018.10.048](https://doi.org/10.1016/j.ceramint.2018.10.048)
- [42] K. Sharma and P. Sharma, Impurity effect of La on Co ferrite: synthesis and structural study, *Optoelectronics and advanced materials-rapid communications*, vol. 7, No. 11-12, pp. 887-890, 2013.